3D printing and characterizations of a soft and biostable elastomer with high flexibility and strength for biomedical applications

Emilio O. Bachtiar[1,2], Ozan Erol[1,2], Michal Millrod[3], Runhan Tao[2,4], David, H. Gracias[5,6], Lewis H. Romer[3,4,7], Sung Hoon Kang[1,2,8,*]

[1]Department of Mechanical Engineering

[2]Hopkins Extreme Materials Institute

[3]Department of Anesthesiology and Critical Care Medicine

[4]Department of Biomedical Engineering

[5]Department of Chemical and Biomolecular Engineering

[6]Department of Materials Science and Engineering

[7]Departments of Cell Biology, Pediatrics, and the Center for Cell Dynamics

[8]Institute for NanoBioTechnology

Johns Hopkins University, 3400 North Charles Street, Baltimore, MD 21218, USA

[*]Corresponding author: Sung Hoon Kang (shkang@jhu.edu)

Abstract

Recent advancements in 3D printing have revolutionized biomedical engineering by enabling the manufacture of complex and functional devices in a low-cost, customizable, and small-batch fabrication manner. Soft elastomers are particularly important for biomedical applications because they can provide similar mechanical properties as tissues with improved biocompatibility. However, there are very few biocompatible elastomers with 3D printability, and little is known about material properties of biocompatible 3D printable elastomers. Here, we report a new framework to 3D print a soft, biocompatible, and biostable polycarbonate-based urethane silicone (PCU-Sil) with minimal defects. We systematically characterize the rheological and thermal properties of the material to guide the 3D printing process and have determined a range of processing conditions. Optimal printing parameters such as printing speed, temperature, and layer height are determined via parametric studies aimed at minimizing porosity while maximizing the geometric accuracy of the 3D-printed samples as evaluated via micro-CT. We also characterize the mechanical properties of the 3D-printed structures under quasistatic and cyclic loading, degradation behavior and biocompatibility. The 3D-printed materials show a Young's modulus of 6.9 ± 0.85 MPa and a failure strain of $457 \pm 37.7\%$ while exhibiting good cell viability. Finally, compliant and free-standing structures including a patient-specific heart model and a bifurcating arterial structure are printed to demonstrate the versatility of the 3D-printed material. We anticipate that the 3D printing framework presented in this work will open up new possibilities not just for PCU-Sil but for other soft, biocompatible and thermoplastic polymers in various biomedical applications requiring high flexibility and strength combined with biocompatibility, such as vascular implants, heart valves, and catheters.

Keywords: additive manufacturing; mechanical behaviors; elastomer; biomedical devices

Graphical Abstract:

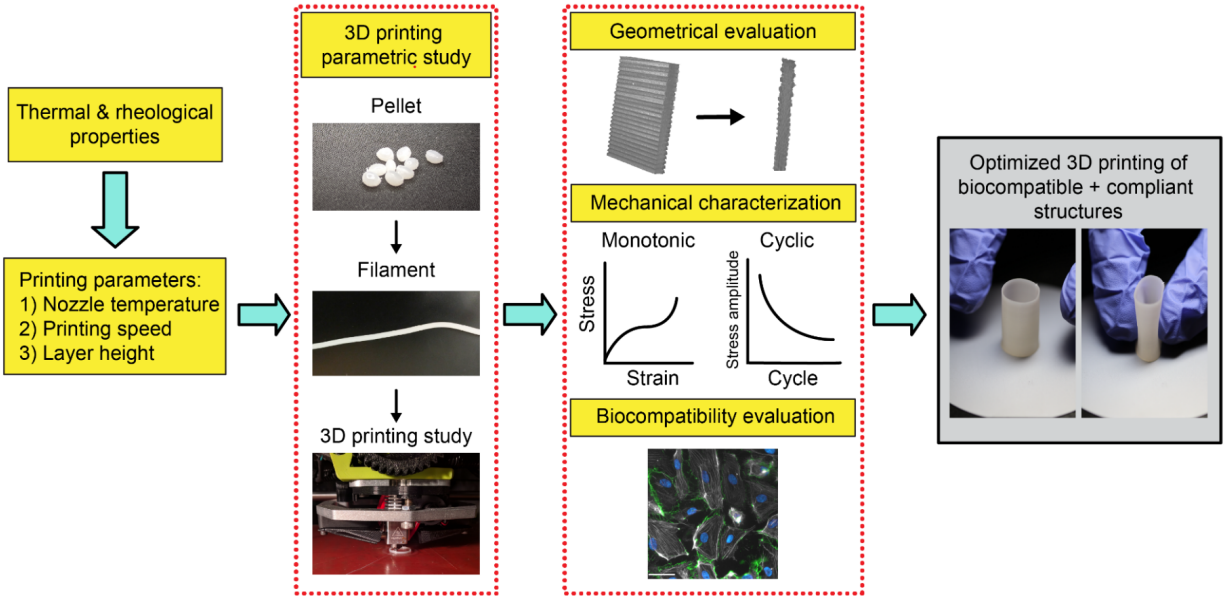

1. Introduction

Recently, 3D printing (3DP) technologies have been widely utilized in biomedical applications because of their ability to fabricate complex shapes that are either impractical or unachievable with conventional manufacturing methods. 3DP has contributed to the development of patient-specific models[1,2], drugs[3], prosthetics, orthopedics[4], and cardiovascular implants[5]. 3DP has become a particularly important tool for patient-specific models and devices since the anatomical features are different widely within the body as well as from patient to patient. Hence, 3DP methods coupled with patient specific imaging such as computed tomography (CT) and magnetic resonance imaging (MRI) have been utilized to personalize medical devices and surgical procedures to improve patient outcomes[6–8].

Commonly used 3DP methods in medical devices include fused filament fabrication (FFF), direct ink writing (DIW), and stereolithography (SLA)[9]. Among these methods, FFF is the most commonly used approach due to its accessibility and ease of use. In FFF, thermoplastic materials are melted and extruded through a nozzle in a layer-by-layer manner to fabricate complex 3D geometries[10]. FFF provides a highly scalable, low-cost, and versatile platform, and has been previously used to print relatively stiff and biocompatible thermoplastics for biomedical applications[10,11]. SLA is a light-based method where a liquid resin is photopolymerized layer-by-layer with a light source. SLA 3DP can achieve high dimensional accuracy and resolutions. However, it suffers from additional processing steps and a limited number of material options that tend to be toxic to cells. DIW is another common extrusion-based 3DP method where a material with an appropriate shear-thinning and thixotropic rheological properties is extruded through a syringe and deposited onto a substrate to form 3D structures. It requires ink formulations with additives to achieve these properties such that they can change their viscosity during extrusion and maintain their shapes after printing. Even though DIW has opened up new possibilities for 3D printing of materials like ceramics[12] and glass[13], it generally suffers from low dimensional accuracy and the need for post-processing steps such as UV curing to obtain the final structures. Moreover, currently available biocompatible materials for DIW have issues such as low toughness, low elastic modulus, and high degradability[14,15].

3D printed soft materials with similar mechanical properties to native tissues and low degradability would be beneficial for various medical devices such as implants, and patient-

specific phantoms for surgical planning. Some examples of these devices include cardiovascular grafts[16] and knee arthroplasty implants[17]. Although tougher and more stretchable hydrogels were recently developed[18], their strengths are much lower than those of typical thermoplastic elastomeric materials[19], making them unsuitable for certain medical applications such as knee implants.

Most biocompatible materials available for FFF are relatively stiff[20]. These materials include poly(lactic acid) (PLA) and polycaprolactone (PCL), with elastic moduli in the range of 2.5 GPa and 0.35 GPa[21], respectively. However, many functional structures in the human body are soft tissues, making stiff materials typically used with FFF unsuitable for medical implants due to the mismatch in mechanical properties. Elastomeric materials have gained significant interest in biomedical research in recent years because of their similar mechanical properties to soft tissues.[22,23] Elastomers are a class of polymers that can rapidly recover from deformation with minimal hysteresis.[24] They also provide low elastic moduli and high failure strains[25]. They are especially beneficial for biomedical applications because of their tunable properties that can be matched to the mechanical properties of biological tissues.[26,27] This is critical for many biomedical applications since mismatches in mechanical properties between native tissues and medical devices may lead to reduced device longevity in applications such as vascular grafts[28], intracortical brain implants[29], and skeletal implants[30].

Thermoplastic polyurethane (TPU) is a suitable material for applications requiring soft elastomeric properties[31,32]. TPU is a physically crosslinked block copolymer with chains composed of both soft amorphous and hard crystalline regions[33]. The hard segments are typically formed out of diisocyanate and diols, which join to the soft segment through urethane linkage[33]. The soft segment consists of long flexible macrodiols, such as ester, ether, and carbonate groups, resulting in polyester, polyether, and polycarbonate-urethanes, respectively[33]. The hard segments undergo a phase separation due to thermodynamic favorability and form hydrogen bonds which result in distinct hard regions that are distributed throughout the soft regions. Regional heterogeneity and hard-soft interactions act as physical crosslinks, providing TPU both high elasticity and thermoplastic nature[33]. Thermoplastic characteristics of TPUs make them ideal candidates for extrusion-based 3D printing methods such as with FFF. Besides, a variety of mechanical properties and the degree of biocompatibility and biostability[34] can be achieved by varying the hard-to-soft

segment ratio, the chemistry and molecular weight of the segments, and processing methods[35–37].

Polycarbonate-based polyurethane silicone (PCU-Sil) is a class of TPU made by co-polymerizing silicone with polycarbonate-urethane (PCU). Pure silicones lack the mechanical integrity required for certain medical devices, but copolymerization with polycarbonate-urethane maintains thermoplastic properties while providing improved mechanical properties such as softness and stretchability, synergistic improvements in biocompatibility, and reduced susceptibility to metal ion oxidation[38,39,40]. The copolymers exhibited silicone-like surface properties with silicone contents as low as < 1%[41]. This is particularly important since the availability of silicone on the material surface inhibits the biodegradation that begins at the surface level[40] and it improves desirable properties such as low toxicity and good blood compatibility[42]. A recent study showed that the thermoplastic property granted by copolymerization allows for 3D printing of PCU-Sil for medical applications[43].

In this work, we report a versatile framework to obtain the optimal processing conditions for soft and biocompatible silicone-polyurethane copolymers to 3D print free-standing and compliant structures with minimal defects and high biocompatibility. We specifically focused on PCU-Sil and systematically characterized the thermal and rheological properties to determine the possible ranges of 3D printing processing conditions for extrusion-based FFF. Guided by the rheological and thermal characterizations, we further determined the optimal printing conditions through a parametric study utilizing microcomputed tomography (micro-CT) aimed at minimizing microstructural defects while improving geometric fidelity. Then, we studied the mechanical properties of the 3D-printed PCU-Sil under quasistatic and cyclic loads to determine its suitability for load-bearing biomedical applications. We further demonstrated the biostability and biocompatibility of the 3D-printed PCU-Sil using in-vitro assays. Finally, we 3D-printed geometrically complex parts to demonstrate the framework's ability to 3D print compliant and biocompatible structures for biomedical applications.

2. Materials & Methods

2.1 Materials and processing

PCU-Sil (ChronoSil, AdvanSource Biomaterials) was purchased in the pellet form. All the

materials were used as received without any further modifications. To make filaments for FFF, the pellets were dried in a vacuum oven (Lindberg Blue M, Thermo Fisher Inc.) at 25 inHg of vacuum at 80 ^{o}C for at least 24 hours. Dried PCU-Sil pellets were then extruded through a 3 mm nozzle with a single-stage single-screw extruder (Filabot EX2, Triex LLC.) at 210 ^{o}C. The resulting filament diameter was 2.47 ± 0.061 mm. Both pellets and filaments were stored in a desiccator box after processing and dried at 80 ^{o}C for 24 hours before conducting any characterizations as well as 3D printing to prevent a moisture absorption effect of creating significant porosity in 3D printed samples.

2.2 Thermal and rheological characterization of PCU-Sil

The materials were melted, extruded through a nozzle and deposited onto a substrate during FFF-based 3D printing. Hence, the thermal and temperature-dependent rheological properties of the PCU-Sil were characterized by TGA, DSC and oscillatory rheological tests to guide the printing process as follows.

2.2.1 Differential scanning calorimetry (DSC)

Differential scanning calorimetry (DSC) was performed in a nitrogen environment using a Discovery Q2500 DSC (TA Instruments, Inc.) to characterize the thermal characteristics such as glass transition temperature, melting temperature and degradation temperature. The samples were weighed and placed in a pan (Tzero Pan, TA Instruments, Inc.). The same pan type was used as a reference for all the experiments. A single thermal cycle including (1) cooling down the specimens to -85°C at 10°C/s with a two-minute isothermal equilibrium, (2) heating up to 260°C at 10°C/sec with a two-minute isothermal equilibrium, and (3) another cooling cycle to -85°C at 10°C/sec was applied to the materials. Each sample was subjected to the same thermal cycling two times. The first heating and cooling cycle erases the sample's thermal history as it is melted and cooled. At the end of each test, samples were removed and re-weighed to evaluate for possible mass changes. None of the samples exhibited mass loss due to thermal cycling during the experiments. Three samples were tested for each case.

2.2.2 Thermogravimetric analysis (TGA)

Thermal degradation and mass loss of both PCU-Sil pellets and filaments were investigated

using a thermogravimetric analyzer (TGA 8000™, PerkinElmer). The temperature of the specimens was increased from 30 °C to 650 °C at 10 °C/min while continuously measuring the sample mass. All samples were tested in a nitrogen environment with three replicates.

2.2.3 Rheological characterizations

Rheological measurements were performed with a rotational rheometer (MCR-9, Anton-Paar Instruments). A parallel plate-to-plate setup with a 1 mm gap and furnace capable of varying the environment temperature was employed during all the experiments. Rheology measurements were conducted at temperatures between 160 °C and 260 °C with 20 °C increments. For each temperature level, a frequency sweep was conducted spanning from 1 rad/s to 100 rad/s at a constant 0.5% shear strain in three replicates.

2.3 Determination of optimal 3D printing parameters

To determine the optimal 3D printing parameters, samples were evaluated by micro-CT after 3D printing as described below.

2.3.1 3D Printing

PCU-Sil filaments were printed using a FFF 3D printer (Lulzbot Taz 6, Aleph Objects) equipped with a direct-drive extruder utilizing a 0.35 mm nozzle (Flexystruder V2, Aleph Objects). To determine the optimal printing conditions, all printing settings except nozzle temperature, printing speed, and layer height were kept constant (See **Table S1**, Supporting Information). All prints were done at room temperature with a relative humidity of < 25%. Before printing, the print bed was covered with a painter's tape (ScotchBlue, 3M) which was then coated with an acid-free glue stick (All Purpose Glue Stick, Elmer's) to improve print adhesion and removal.

2.3.2 Micro-CT evaluation of printed specimens

Print quality was evaluated by printing single-walled hollow boxes with 15 mm × 15 mm dimensions. The printed samples were cut into square sheets (7.5 mm × 7.5 mm) and scanned with micro-computed tomography (micro-CT) (SkyScan 1172, Bruker micro-CT) to investigate the printing quality as a function of printing parameters. Scans were done at 10 μm/pixel and 0.25° rotational increments for all samples. Scan voltage and current were set at 70 kV and 141 μA,

respectively. Exposure time was set to 100 ms for all scans. Morphometry evaluation and 3D reconstruction were conducted with reconstruction software (CTan, Bruker micro-CT).

2.4. Mechanical characterizations

Mechanical properties of the 3D-printed samples were evaluated under quasistatic and dynamic loading conditions as described below.

2.4.1. Quasistatic testing

The mechanical behavior of the 3D-printed materials was investigated with quasistatic tensile tests. Tensile dogbone samples were directly 3D-printed based on the geometrical guideline from the ASTM D638 standard (Type IV)[44]. Dogbones were printed with a shell of 2 × 0.3 mm along its border. Printing parameters used for all the specimens are summarized in **Table S1**. The effect of the printing direction was investigated by 3D printing specimens with different raster angles including 0^o (printing direction aligned with loading), 90^o (printing direction perpendicular to loading), $45^o/45^o$ and $0^o/90^o$ with 10 layers. All specimens were tested in air at room temperature using a universal tensile test machine (MTS Criterion Model 43, MTS Inc.) with a 5 kN load cell. Spring-loaded roller grips were employed for all tests to prevent slippage at the clamps. Crosshead displacement speed was set at 50 mm/min and force-displacement curves were recorded at 1 Hz. For each experiment, at least three specimens were tested.

2.4.2. Cyclic testing

Cyclic tests were conducted to determine the fatigue life of the 3D-printed specimens. Tensile dogbone specimens (Type V) were 3D-printed based on the ASTM D638 standard[44]. All specimens were 3D-printed similarly as the quasi-static tensile test specimens with a 0^o raster angle. The tests were conducted using a load-controlled tensile test machine (Instron E1000, Instron Inc.) with a 250 N load cell in a pulsating tension manner where the minimum load was set to 0 N. Four mean stresses (0.5, 0.75, 1.0 and 1.5 MPa) within the linear elastic region of the material were used to develop the fatigue curves with five replicates. ASTM D7791 standard (Standard test method for uniaxial fatigue properties of plastics) was followed for the experiments whenever possible[44]. The samples were loaded using a sinusoidal waveform at 5 Hz at room temperature in air. The runout for the experiments was set to 10^6 cycles.

2.5 Degradation in physiological conditions

Hydrolytic degradation of the 3D-printed materials under physiological conditions was investigated using an ASTM F1635 standard[44]. Dogbone samples (ASTM D638 Type IV) were printed similarly to the quasi-static tensile test specimens. The printed samples were dried overnight at 80 ^{o}C to remove moisture and their mass was recorded using an analytical balance (ME-T Precision Balance, Mettler-Toledo, Inc.). Each sample was then completely immersed in a separate glass tube filled with phosphate-buffered saline (PBS) solution (Sigma-Aldrich). The pH level of the PBS solutions was maintained at 7.4 ± 0.2 throughout the experiments. The samples were placed in a forced-air convection oven (Quincy 10GC, Quincy Labs) at 70 ^{o}C to accelerate the degradation rate based on the ASTM F1635 standard. The test was conducted for four weeks and four samples were removed each week to determine the mass loss and the changes in the mechanical properties as a function of degradation time. Quasistatic tensile tests were conducted immediately after the removal of samples from PBS to determine the changes in mechanical properties. To determine the mass loss, the immersed samples were removed from PBS and dried at 80 ^{o}C over a maximum period of 48 hours. Mass of the specimens was remeasured after PBS was completely removed from the specimens and compared to their initial masses to determine the degree of mass loss due to hydrolytic degradation.

2.6 Biocompatibility experiments

The biocompatibility of the printed materials and processes was tested by following the ISO 10993-5 standard (Biological evaluation of medical devices - Tests for *in-vitro* cytotoxicity)[45].

2.6.1. Extract preparation & material cytotoxicity

Non-contact cytotoxicity experiments were conducted to determine the toxicity of the materials. Pellets of PCU-Sil, 3D-printed PCU-Sil, and latex samples were initially sterilized by immersing them in 70% ethanol for 30 minutes and triple rinsing with sterile Phosphate-buffered saline (PBS, Gibco). The samples were then incubated in Endothelial Cell Growth Medium MV2 (EGMV2, Promocell) supplemented with Penicillin Streptomycin (Corning) at 37 ^{o}C with 5% CO_2 to extract leachables and prepare the conditioned media (CM). The material surface area to extraction fluid volume was equal to ~6 cm^2/mL for all samples based on ISO 10993-12 standard

(Sample preparation and reference materials). The supernatant was collected at the end of 72 hours and stored at 4 ºC until further use. Latex was chosen as a positive control based on the previous studies[46]. EGMV2 alone was also incubated under the same conditions as a negative control.

Human pulmonary microvascular endothelial cells (HPMEC) were obtained from Promocell and seeded onto a 96-well plate at a density of 10^4 cells/cm^2 and cultured for 24 hours. Then, the medium was extracted from the wells and the CM containing leachables from each material was added to the wells. The plate was incubated at 37 ºC in 5% CO_2 for seven days while replacing the CM with fresh CM on days three and six. Cells with regular growth media were also cultured as one of the controls. On day seven, the supernatant was collected to quantify nitric oxide (NO) production and the cells were frozen to determine material cytotoxicity. The standard CyQuant Cell Proliferation Assay (Invitrogen) was employed to study the toxicity of the materials. Frozen cells for each condition were thawed and lysed by following the CyQuant assay protocol. The fluorescence emission was determined with a SpectraMax Gemini EM microplate reader (Molecular Devices) with ~480 nm excitation and ~520 nm emission maxima. Fluorescence measurements were converted to the number of cells using a standard curve.

2.6.2. Nitric oxide (NO) production quantification

NO production of the HPMEC was quantified by analyzing the supernatant collected on day seven of the cytotoxicity experiments. The concentrations of the primary oxidation product nitride (NO_2) were determined using chemiluminescence with a Sievers Nitric Oxide Analyzer (Sievers Instruments, Boulder, CO). Supernatants with NO_2 were reduced with potassium iodide in acetic acid to NO which was then quantified with NO analyzer after reaction with ozone. The amount of NO produced for each condition was normalized using the number of cells obtained from the CyQuant assay.

2.6.3. Histological staining for endothelial activation

Endothelial activation effects of the materials were determined using fluorescence imaging. The HPMECs were seeded onto 12 well plates containing glass coverslips coated with human fibronectin (25 ug/ml) (Gibco) with a seeding density of 1.5×10^4 cells/cm^2. The cells were fed with CM on days one, three and six in a similar manner to that used for the cytotoxicity experiments.

Cells were also grown with regular cell media in wells. For a positive control, 50 ng/ml of IL1-β (PeproTech) was added to the cells grown with regular growth media on day six to activate the HPMEC. On day seven, glass slides were fixed and permeabilized with 0.5% Triton X-100 in 3% methanol-free paraformaldehyde. For immunofluorescence labeling, rabbit polyclonal anti-VE-cadherin (1:100) (Cayman Chemicals) and mouse monoclonal anti-phosphotyrosine (1:50) (BD) were used as primary antibodies. Alexa Fluor 488 conjugated donkey anti-rabbit IgG (1:100)(Life Technologies) and cy3 goat anti-mouse IgG (1:100) (Jackson ImmunoResearch) were used as secondary antibodies. Conjugated F-actin 647 (1:50) (Life Technologies) and DAPI (1:50) (4′,6-diamidino-2-phenylindole; Thermo Fisher Scientific) were also used. Slides were imaged with a Nikon Eclipse TE200 microscope using Volocity software (Quorum Technologies).

2.7 Statistical analysis

All experiments were repeated at least three times unless noted. All statistical analysis was performed using JMP (SAS Institute, Inc.). Statistical differences were determined with analysis of variance (ANOVA) and Tukey-Kramer tests with a 95% confidence interval for all experiments.

3. Results and Discussion

3.1 Thermal and rheological characterization of PCU-Sil

The materials were melted, extruded through a nozzle and deposited onto a substrate during FFF-based 3D printing. The thermal and temperature-dependent rheological properties of the PCU-Sil were characterized using TGA, DSC, and oscillatory rheological tests to guide the printing process.

3.1.1 Differential scanning calorimetry (DSC)

Fig. 1a shows a representative DSC curve of PCU-Sil where the samples from pellets and filaments were subjected to two consecutive heating-cooling cycles. The glass transition temperature was reported as being the midpoint temperature of a second-order transition in the thermogram, with the first pass glass transition marked T_{g1} and second pass glass transition marked T_{g2} (**Table 1**). The temperature at which the sample goes through enthalpic relaxation is marked as T_1 and melting endotherm region is marked as T_{mh}. Both pellet and filament samples had a glass

transition temperature around -30 °C, which is common with polycarbonate-urethane based polymers and attributed to the behavior of soft segments[19,37,50]. The samples also showed a pronounced endothermic peak around 105 °C during the first cycle. This endothermic peak was attributed to the physical aging of the polymer which is commonly seen in amorphous polymers over its storage period, causing enthalpic relaxation as it is heated[51,52]. After the first melt cycle, the physical aging effect was diminished where no endothermic peaks were observed around 105 °C. A possible effect of moisture was ruled out by weighing the samples using an analytical balance. TPUs typically show a wide melting endotherm associated with the melting of the hard domain, which was not observed (**Fig. 1a**). The absence of the melting endotherm indicates that the hard segment content of the PCU-Sil is lower. However, the first-order transition at around 160 °C was still observed, which corresponds to a typical melting endotherm for PCUs[19,37,50].

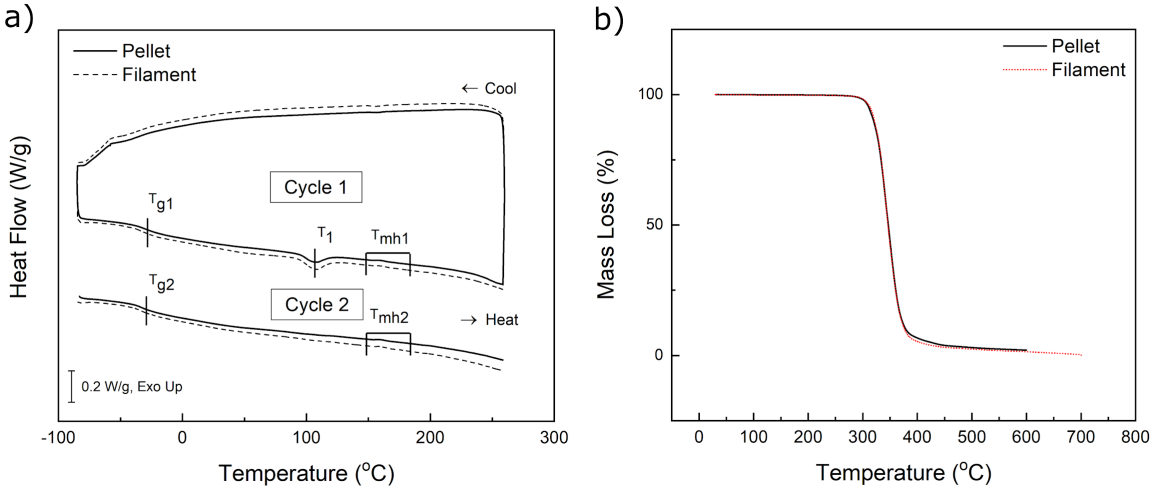

Figure 1. a) Representative DSC curves for PCU-Sil pellet and filament. An exothermic reaction is in the upward direction. b) A representative TGA thermogram of PCU-Sil pellet and filament.

Table 1. The average value and standard deviation of DSC thermogram features for PCU-Sil pellet and filament samples.

Sample Type	**T_{g1}** (°C)	**T_{g2}** (°C)	**T_1** (°C)
Pellet	-28.6 ± 0.44	-28.0 ± 0.35	104.2 ± 2.17
Filament	-30.6 ± 0.03	-30.1 ± 0.16	100.0 ± 0.44

3.1.2 Thermogravimetric analysis (TGA)

The thermal stability of pellets and filaments was determined with thermogravimetric analysis (TGA). The start of the thermal degradation is particularly important since the materials are melted and extruded at different temperatures during both the filament making process and the 3D printing process. **Fig. 1b** shows the average TGA thermogram curves of PCU-Sil pellets and filaments, showing a typical single-stage decomposition process, suggesting good phase-mixing[47] which was similarly shown by the DSC thermogram. Significant weight loss is observed at temperatures higher than 300 ^{o}C, indicating that printing temperature should be selected below 300 ^{o}C temperature to avoid significant thermal degradation.

3.1.3 Rheological measurements

The rheological properties of the PCU-Sil were characterized using a rotational rheometer at different temperatures between 160 ^{o}C and 260 ^{o}C with 20 ^{o}C increments. The upper limit was chosen as 260 ^{o}C since PCU-Sil started exhibiting significant thermal degradation above this temperature based on the TGA results (**Fig. 1b**). Complex viscosity of the PCU-Sil filaments is measured at different temperatures as a function of angular frequency. A previously developed analytical model for a direct drive extruder was employed to estimate the ranges of possible shear rates that PCU-Sil can undergo during extrusion (See **S2**, Supporting Information)[48]. Printing speeds ranging from 1 mm/s to 50 mm/s with a 0.35 mm nozzle diameter were used to determine the range of angular frequencies that the material experiences during printing. The analytical apparent shear rates (angular frequencies) obtained from the model based on the Cox-Merz rule, were ranged between 20 s^{-1} and 1100 s^{-1}. Even though the oscillatory shear rheometers cannot reach the angular frequencies above 100 rad/s, the complex viscosity of the polymer melt can be estimated via temperature-time superposition (TTS) [49]. Hence, master curves using Arrhenius relation were constructed for the temperatures studied to determine the viscosities at higher angular frequencies[50]. **Fig. 2** shows the master curves generated for a reference temperature of 260 ^{o}C and the estimated viscosities at higher angular frequencies. Shift factor values used for TTS is shown in **Table S2**. Raw viscosity measurement data at various temperatures is shown in **Fig S1.** The viscosity of the PCU-Sil melts decreased as the temperature increased. Viscosity was dependent on the angular frequency and decreased as the applied angular frequency increased, suggesting shear-thinning properties that are commonly seen in polymer melts[51].

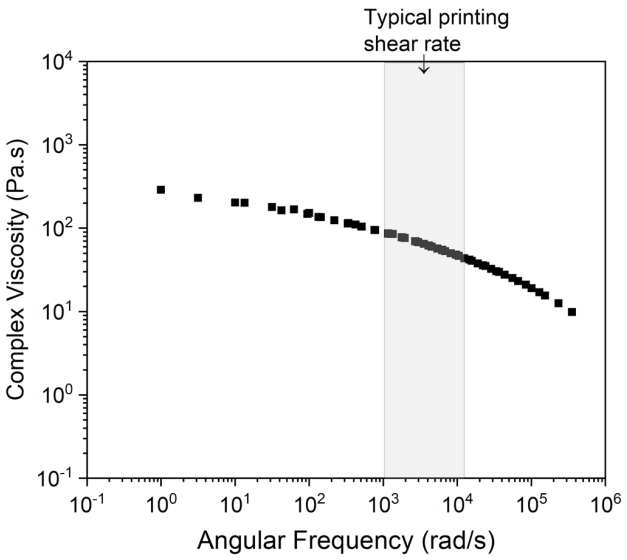

Figure 2. Rheological properties of the PCU-Sil filaments as shown by a master curve of PCU-Sil melt determined from TTS with a reference temperature of 260 °C.

3.2 Determination of optimal 3D printing conditions

3.2.1. Micro-CT measurements

The microstructures and the porosity of 3D-printed structures were quantified with micro-CT as a function of printing parameters. There is a large number of parameters that can be used in 3D printing including, but not limited to printing temperature and speed, nozzle temperature, layer height, infill pattern, environmental parameters (temperature and humidity), and cooling speed. These parameters play important roles and can be tuned to improve the geometrical, mechanical and surface properties of 3D-printed parts. The current work particularly focused on three important parameters: (1) printing speed, (2) nozzle temperature, and (3) layer height since these parameters have been previously shown to have a significant impact on the printing quality[52,53]. During the study, all other parameters were kept constant (See **Table S1** in Supporting Information for details).

Single-walled hollow cubes were 3D printed and scanned using a micro-CT with a resolution of 8.5 μm/pixel to reconstruct 3D models. **Fig. 3** shows the 2D cross-sections obtained from micro-CT scans. Distinct differences were observed between the cross-sections printed with different printing parameters. Differences were particularly seen in, (1) porosity, (2) over- and

under-extrusion, and (3) geometric dimensions of the printed parts. Hence, these different parameters were employed to quantify the printing quality. Porosity was directly determined from the reconstructed models obtained from the micro-CT. Over- and under-extrusion constant for the prints were calculated by comparing the targeted volume of the object from the CAD model to the actual volume of the 3D-printed sample (See **S4** in Supporting Information). Values beyond the reference value were indicated as over-extrusion and vice versa, for under-extrusion. Besides, a geometric variance was calculated to quantify the variance of the 2D cross-section (See **S5** in Supporting Information). **Fig. 4** summarizes the porosity, over-/under-extrusion, and geometric variance of the 3D-printed objects in the form of a heatmap to assist in identifying trends. A lighter shade in the heatmap indicates better print quality.

A trend of reduced geometric variation was observed with an increase in printing temperature and a decrease in speed as indicated by lighter colors in **Fig. 4a** and **Fig. 4b**. This observation is in line with past studies showing a similar trend wherein fibers extruded at higher temperatures exhibit better wetting and molecular diffusion between the layers[54] and improving mechanical properties[55,56]. While hot-end temperature directly affects the extruded fiber's temperature, the effect of lower print speed is less obvious. This was attributed to the lower print speed resulting in a higher thermal mass of the fibers due to the longer residence in the hot-end. Although radiant heat transfer could also contribute to this, Seppala *et al.* has shown the increase to be relatively small[57]. Furthermore, flow instability at high shear may be a contributing factor[58,59]. The lowest geometric variance value was observed for objects printed at 240 ^{o}C printhead temperature, 5 mm/s printing speed and 0.15 mm layer thickness. This is confirmed visually in **Fig. 3** where it is observed that the cross-section is indeed uniform as indicated in **Fig. 4b** by a white square. At 280 ^{o}C, microscale pores were also observed, with the worst case showing up to 2.46% porosity (for parameters of 280 ^{o}C, 17 mm/s speed, 0.15 mm layer height). These pores were more prevalent at very high print temperature and very low print speed of 1 mm/s. Higher temperatures and lower speeds resulted in higher porosities, as shown in **Fig. 4c** and **Fig. 4d** by darker shades. A similar phenomenon was observed in a past study with ABS and ABS composites[60], potentially indicating that the material is degrading when subjected to a prolonged stay at a high temperature. Bellehumeur *et al*. have also shown the evolution of deposited ABS filament towards an irregular contour with prolonged exposure at a high temperature which was attributed to thermo-oxidative thermal degradation[54]. The pores and other irregularities are

possibly created by gas emission from the degradation process or through other degradation modes. Instances of thermal degradation caused by the 3D printing process have also been observed in past studies involving PLA, PCL, and PLGA[61,62]. It is further supported by the TGA measurements done in this study.

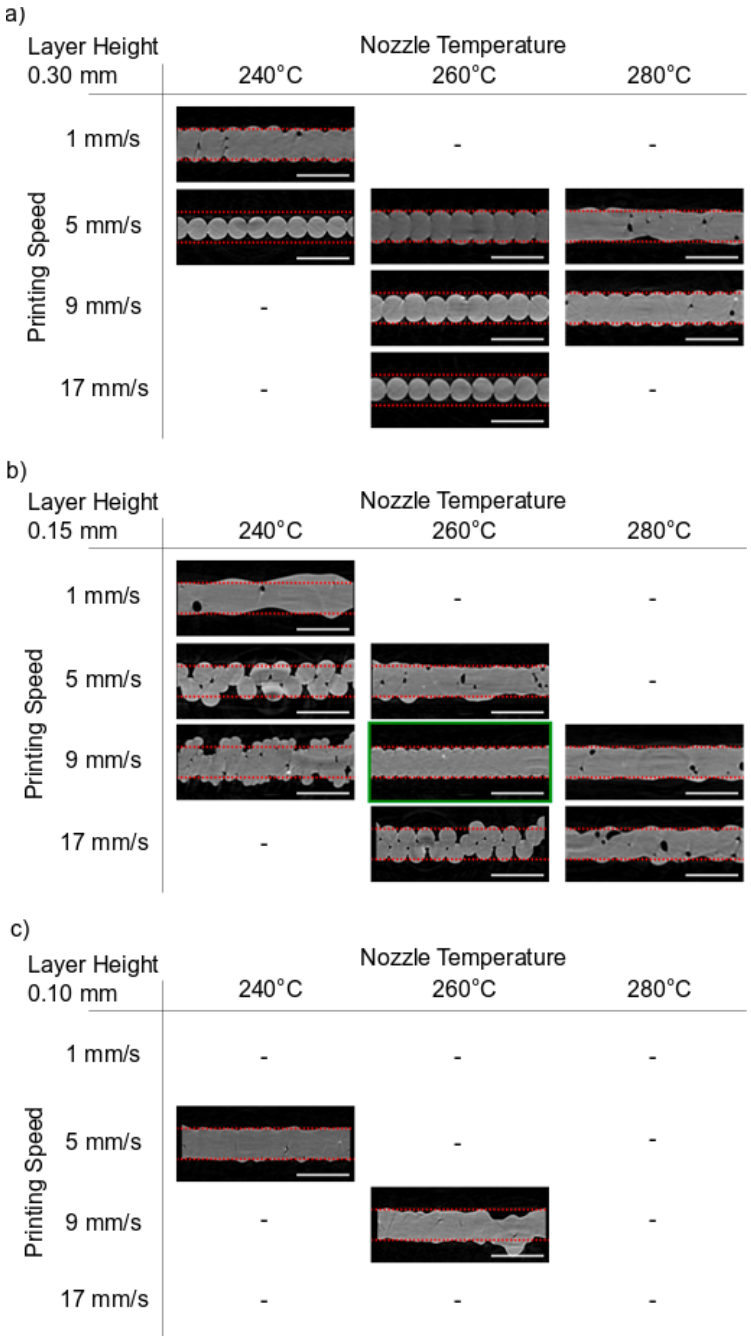

Figure 3. 2D cross-section images of 3D-printed objects using different printing parameters, taken by micro CT. a) Objects with 0.3 mm layer height, b) objects with 0.15 mm layer height, c) objects

with 0.10 mm layer height. (Image with a green border indicates the chosen optimal printing parameter. Red dotted borders indicate the intended structure thickness of 0.35 mm. Scale bar represents 0.5 mm. The absence of any image indicates that objects were not printable with the prescribed parameters.)

Another important feature observed was that certain cross-sections exhibited smaller total areas compared to others (**Fig. 3**). Printing at a higher speed and a lower temperature resulted in under-extrusion, as shown by **Fig. 4e** and **Fig. 4f** by darker shades. The red striped line in **Fig. 3** indicates the target width of 0.35 mm, which was not achieved at higher printing speeds. Most of the printed objects tend to be under-extruded. This was attributed to the higher pressure drop at the printing nozzle for print parameters with higher flow rates, causing difficulty in achieving the targeted material extrusion rate. The high viscosity of the molten filament leads to high pressure levels in the nozzle, which can lead to slippage between the extruding gear and the filament[53]. The slippage between gear and filament inhibits the piston action which pushes the molten polymer out of the hot end, causing under-extrusion[63,64]. Under-extrusion is more pronounced in larger layer heights since higher polymer flow would require higher heat flow for printing. This is indicated by the overall darker shades for **Fig. 4e** compared to **Fig. 4f**. The cross-section of objects printed at 240 °C, 0.15 mm height, and 9 mm/s were significantly different compared to other conditions, showing at first glance, a case of extreme over-extrusion as indicated by its large volume measurement. Rather, this was caused by layers collapsing and lateral overlap due to poor layer adhesion caused by insufficient nozzle temperature.

Low-quality prints and complete print failures were attributed to (1) insufficient heat resulting in high polymer melt viscosity, (2) excessive heat resulting in very low polymer viscosity. At very high viscosity (i.e. low temperature), the polymer is too viscous to be extruded properly, which leads to under-extrusion or poor bed adhesion, leading the print to fail entirely[65,66]. On the other hand, excessive heat causes the molten polymer to degrade and very low viscosity causes the polymer to not solidify properly during printing. In this study, a parameter of 260 °C printing temperature, 0.15 mm layer height, and 9 mm/s speed is used due to minimizing the geometric deviation of the cross-section while maintaining close to zero porosity, albeit with a slight under-extrusion.

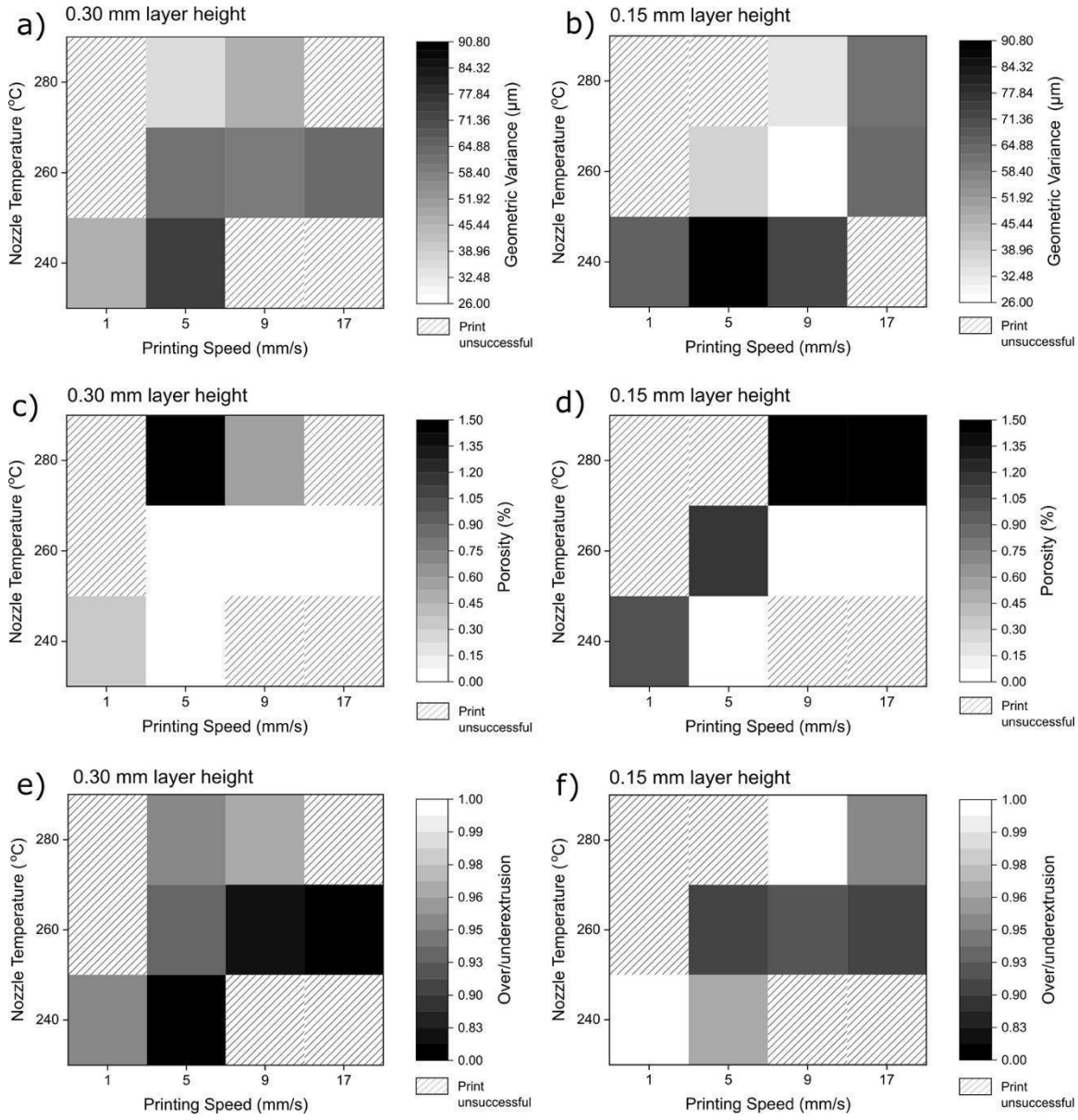

Figure 4. Heatmap plot of different parameters used to quantify print quality. The layer height of 0.10 mm was excluded due to the small number of data points. a,b) Plot showing the geometric variance of objects printed at 0.3 mm and 0.15 mm layer height, respectively. c,d) Plot showing porosities of objects printed at 0.3 mm and 0.15 mm layer height, respectively. e,f) Plot showing the over-/under-extrusion ratio of objects printed at 0.3 mm and 0.15 mm layer height, respectively. A ratio of 1 indicates an ideal print (i.e. printing result is as instructed via software). Unsuccessful prints are indicated by diagonally rastered boxes. Higher/lower values are represented by a grayscale color gradient, with a color closer to white being better for print quality.

3.3. Characterization of mechanical behavior of 3D-printed materials

3.3.1. Quasi-static mechanical behavior

The quasi-static uniaxial tensile stress-strain curve of the 3D printed PCU-Sil samples is shown in **Fig. 5a.** The printed material demonstrates a typical elastomeric behavior with an initial linear elastic region followed by a non-linear behavior. Its initial stress-strain response is followed by strain-softening starting at around 30% strain, then exhibiting strain hardening starting at around 250% strain. The resulting stress-strain curve was shown to be comparable to more common TPU chemistries such as PCU and PEU[67]. Besides, the printed materials exhibited a change in their mechanical behavior depending on the resting time (See **S5** in Supporting Information). This was attributed to the physical aging of PCU-Sil via phase separation, which was supported by the enthalpic relaxation peak data from the DSC thermogram (**Fig. 1a**). A similar phenomenon was previously observed in other TPU chemistries, such as PCU without silicone soft segment[19]. Hence, the samples were stored at room temperature in a desiccator box over a period of two weeks where the mechanical behavior was stabilized for further testing.

Fig. 5b shows the effect of the printing angles on the mechanical behavior of the printed PCU-Sil samples. 0° raster angle samples were printed with the layers aligned with tensile loading direction while 0°/45° and 0°/90° samples were printed with alternating angles. 0°C raster angle samples showed the highest Young's modulus and ultimate tensile strength (UTS) while 90° raster angle specimens exhibited the lowest values. This is caused by the exerted tension directly acting on the printed weld lines in the 90° raster angle specimens, which has been observed in previous studies of FFF 3D-printed rigid polymers[68,69].

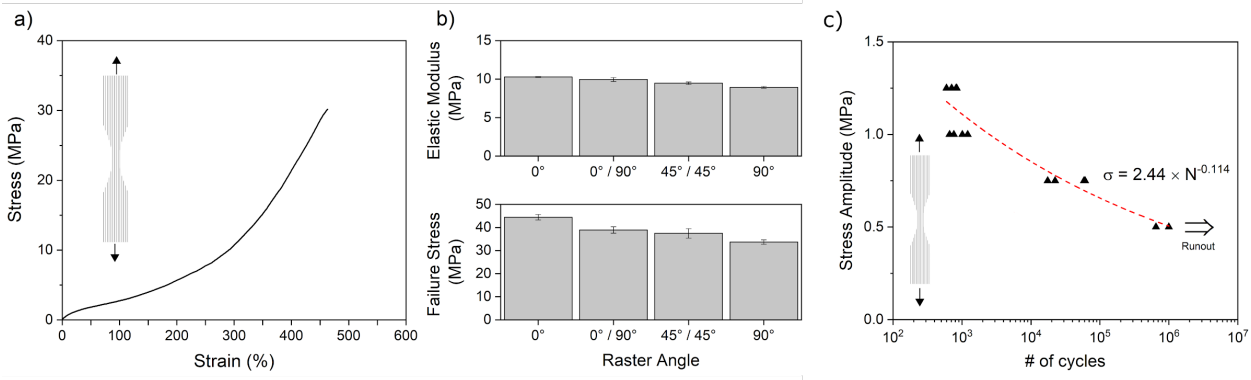

Figure 5. Quasistatic mechanical behavior of the 3D-printed samples. a) A representative curve

of PCU-Sil printed at 0° raster angle from a uniaxial tension test. b) Failure stress and elastic modulus of samples printed at various raster angles. c) Fatigue life data of the 3D-printed material based upon the mean stress amplitude. Arrow indicates a runout at 10^6 cycles.

3.3.2. Cyclic mechanical behavior

The fatigue life of the 3D-printed PCU-Sil samples was determined from force-controlled cyclic experiments where the samples were tested under pulsating tension with prescribed minimum stress of zero. **Fig. 5c** shows the fatigue life of the 3D-printed samples based on the mean stress amplitude prescribed for each test condition. A curve fit based on Basquin's equation is done and shown in the figure. The results show that the 3D-printed specimens tested at the mean stress levels of 1.25 MPa, 1 MPa and 0.75 MPa failed before reaching 10^6 cycles which were designated as runout during the experiments. The samples tested at 0.5 MPa mean stress level reached out to the runout at 10^6 cycles.

3.3.3. Mechanical behavior after hydrolytic degradation

Representative tensile stress-strain curves of degraded 3D-printed PCU-Sil samples are shown in **Fig. 6a**. The important features of the curve are summarized in **Fig. 6b**. Statistical analysis of the curves suggests that there was no statistical difference in the sample's mechanical behavior over the period of accelerated degradation study, suggesting a high resistance to hydrolytic degradation. In addition to hydrolytic degradation polycarbonate-urethane (PCU) is also susceptible to other degradation modes such as oxidative degradation[70], albeit to a much lesser degree in comparison to the more common polyether-urethane (PEU)[70,71]. More recent studies have also indicated that the addition of silicone soft-segment to PCU improves oxidative stability even further[72,73], making PCU-Sil a great candidate for a biostable polyurethane mix.

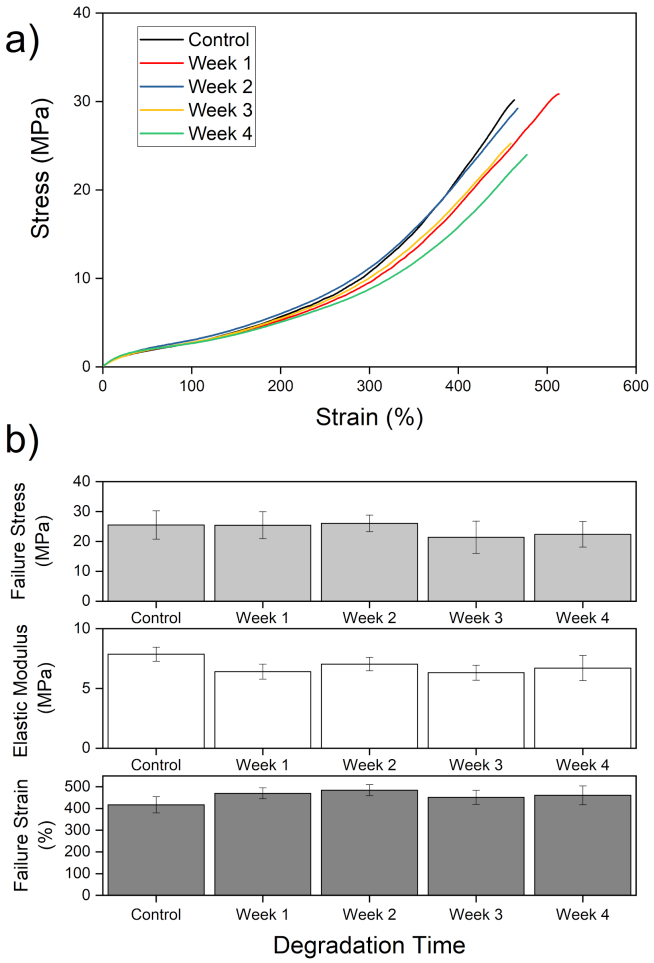

Figure 6. a) Representative tension test curve of PCU-Sil post-degradation in PBS. b) Failure strain, failure stress, and elastic modulus of PCU-Sil after degradation protocol showing no statistically significant difference over 4 weeks. (all p-value pairs > 0.158)

3.4. Characterization of biocompatibility of 3D-printed materials

3.4.1. Material and processing cytotoxicity

Human pulmonary microvascular endothelial cells (HPMEC) were cultured for seven days with standard growth medium (negative control), and with extracts obtained from 3D-printed PCU-Sil, PCU-Sil pellets, and with latex (positive control for known toxicity). **Fig. 7a** shows the cell density at the end of seven days of exposure of the HPMEC to extracts obtained from the tested materials. There was no significant difference between cell viability in standard medium

and in medium containing extracts from PCU-Sil pellets or 3D-printed PCU-Sil ($p<0.05$). These data indicate that exposure to these materials did not result in cell cytotoxicity.

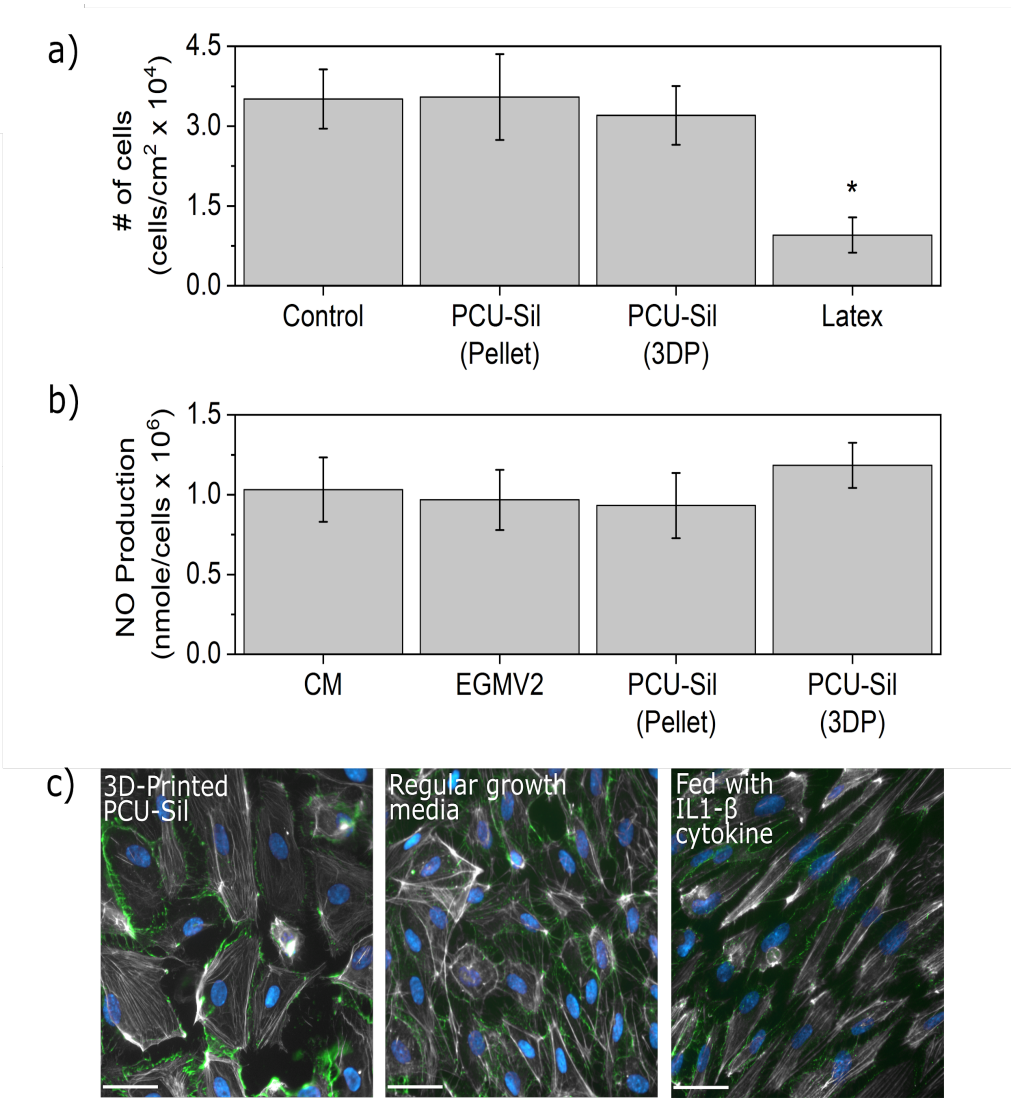

Figure 7. Biocompatibility of the PCU-Sil and 3D printing. a) Cell viability for PCU-Sil pellets, 3D-printed PCU-Sil samples, and controls obtained following a seven-day cell culture (asterisk indicates statistical significance, $p < 0.05$), b) Normalized NO production after seven days in cell culture (no statistically significant differences between all pairs, $p > 0.05$). c) HPMEC activation was not observed upon exposure to PCU-Sil pellets or 3D-printed PCU-Sil samples, as determined by intact VE-cadherin-mediated cell-cell junctions and a quiescent pattern of actin cytoskeletal organization. (All scale bars are 40 μm)

3.4.2. NO production quantification

The function and health of the HPMEC in the presence of the extracts were characterized by quantifying the production of NO, a critical endothelial signaling molecule, using chemiluminescence with a Sievers Nitric Oxide Analyzer. **Fig. 7b** shows the comparison of the NO concentrations measured from the supernatants collected on day seven of the cytotoxicity experiments. These measurements were normalized by the number of cells obtained with the cytotoxicity assay. There were no statistically significant differences in the NO production between the control conditions (cells grown with CM and regular growth media), PCU-Sil pellets, and 3D-printed PCU-Sil samples ($p<0.05$). This finding indicates that the biocompatibility of PCU-Sil pellets and 3D-printed PCU-Sil samples is high and that exposure to these materials does not alter a vital endothelial function.

3.4.3. Histological staining for endothelial activation

Possible endothelial activation due to the presence of material derivatives was examined using epifluorescence imaging. HPMEC grown in regular cell media were compared with those grown in growth medium containing extracts from 3D-printed PCU-Sil. As a positive control, 50 ng/ml of IL1-β (PeproTech) was added to the media of cells grown in parallel samples. **Figure 7c** shows epifluorescence images obtained for the 3D-printed PCU-Sil sample as well as the controls. The images show that microvascular endothelium exposed to the PCU-Sil from the 3D-printed samples exhibited similar quiescent actin cytoskeletal organization and intact VE-cadherin-mediated cell-cell junctions to the cells grown with regular growth media. On the other hand, endothelial cells activated with IL1-β (50 ng/ml) exhibited distinct morphological changes of activation, including cytoskeletal contraction and fragmentation of cell-cell junctions. The results indicate that HPMEC incubated with the growth media containing materials extracts were not activated but rather stayed normally quiescent.

3.5. Demonstrations of 3D-printed compliant structures

Fig. 8 shows examples of compliant structures that were 3D-printed from PCU-Sil. **Fig. 8a** shows a thin-wall tubular structure with a wall thickness of approximately 350 μm. This type of structure could potentially be useful in fabricating medical implants with a need for compliance

and biostability, such as a large-diameter vascular graft or a meniscus implant. **Fig. 8b and Fig. 8c** shows a 17-year-old's heart model fabricated based on data from NIH's model repository[74] and a bifurcated artery, respectively. These examples show the potential use of these 3D-printed compliant structures in surgical planning and personalized devices. **Fig. 8d** shows a flexible twisting arm structure which increases rotation angle as the higher load is placed on the structure, showing an example of structures that are made possible via the printing of soft material, such as shown in this study.

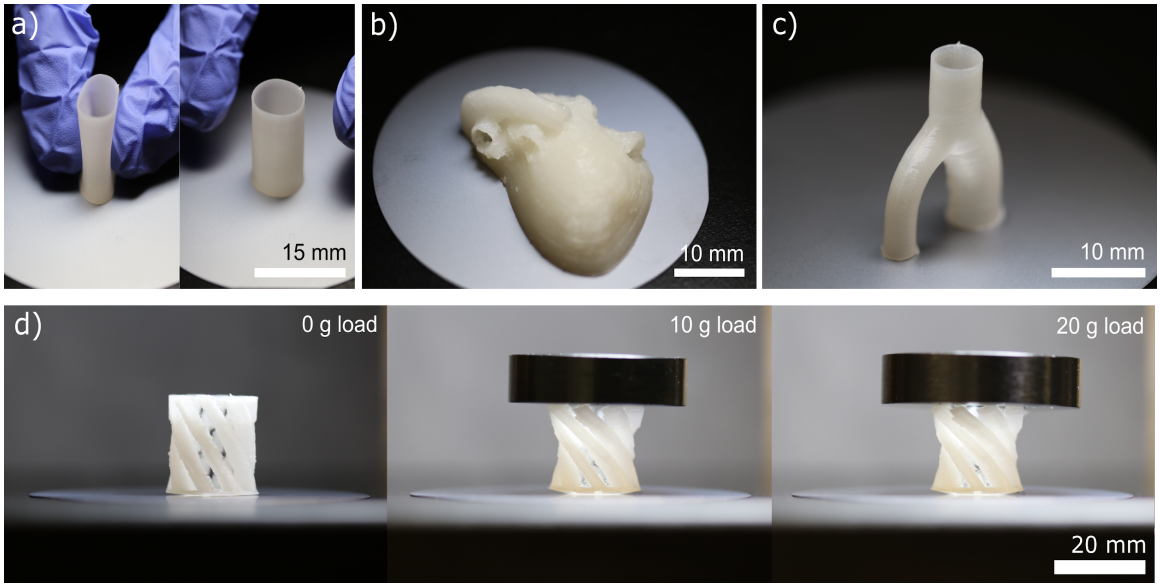

Figure 8. Examples of 3D-printed structures fabricated from PCU-Sil. a) A thin-wall tubular structure exhibiting compliance, b) a patient-specific heart model, c) an arterial bifurcation, and d) a progressively loaded twisting arm mechanism.

4. Conclusions

In this work, 3D printing of a soft and biodurable elastomer (PCU-Sil) and the mechanical behaviors and biocompatibility of 3D-printed specimens were reported. The thermal and rheological properties of the material were evaluated to guide the 3D printing process. Then, 3D printing parameters were systematically investigated to find an optimal set of printing parameters for PCU-Sil, resulting in an ideal print parameter of 260 °C nozzle temperature, 9 mm/s printing speed, and 0.15 mm layer height. These print parameters were determined using micro-CT to result

in objects with minimal porosity and high geometric fidelity. Structures with walls as thin as 300 μm were printed with this approach, showing capability for printing highly compliant structures. Uniaxial tensile tests of the 3D-printed samples showed Young's modulus of 6.9 ± 0.85 MPa at 5% strain and a failure strain of 4567 ± 37.7%, exhibiting soft mechanical properties with good extensibility. 3D-printed dog-bone samples did not exhibit any statistically significant decrease in mechanical properties after an accelerated degradation protocol in PBS, suggesting biostability and thus its use in permanent medical implants. 3D-printed samples were also subjected to fatigue testing to study their cyclic behavior. The result can be used to estimate the fatigue life of the compliant structures and design structures to avoid potential fatigue failures. An *in-vitro* biocompatibility evaluation for cytotoxicity, NO production, and endothelial activation showed that high cell viability without any adverse effects on cell function or cytoskeletal structure were preserved throughout exposure to PCU-Sil.

Some potential limitations in this study include the absence of a biobath in testing mechanical properties. A biobath would give perspective on how PCU-Sil would behave during its implementation as a medical implant, particularly on how its properties could potentially change when immersed in biological fluids and at body temperature. Furthermore, degradation study was done with PBS, thus only exposing PCU-Sil to hydrolytic degradation, and excluding other degradation modes such as oxidative degradation. Nevertheless, the characterization results have indicated that PCU-Sil has much potential for 3D printing of medical implants.

Given the properties assessed in this study, FFF 3D printing of PCU-Sil was found to be a suitable fabrication approach for additive-manufacturing of biostable, biocompatible, and mechanically compliant biomedical devices. We anticipate that the FFF-based 3D printing framework presented in this work will open up new possibilities not just for PCU-Sil but for other soft, biocompatible and thermoplastic polymers in various biomedical applications requiring high flexibility and strength combined with biocompatibility such as vascular implants, heart valves, and catheters.

Acknowledgment

The research reported in this publication was supported by the Eunice Kennedy Shriver National Institute of Child Health & Human Development of the National Institutes of Health

under Award Number R21HD090663, the National Science Foundation (DMR-1709349), the Johns Hopkins University Whiting School of Engineering Start-Up Fund, and Kley Dom Biomimetics. E. O. Bachtiar was supported by the Indonesian Endowment Fund for Education. We acknowledge J. W. Oh for assistance with the cyclic mechanical tests and S. Yao for assistance with the degradation test. The content is solely the responsibility of the authors and does not necessarily represent the official views of the funding agencies.

Data availability

The raw/processed data required to reproduce these findings cannot be shared at this time as the data also form part of an ongoing study.

References

1. Banks, J. Adding value in additive manufacturing: Researchers in the United Kingdom and Europe look to 3D printing for customization. IEEE Pulse. 2013; 4 (6): 22--6. (2013).
2. Mertz, L. Dream it, design it, print it in 3-D: what can 3-D printing do for you? *IEEE Pulse* **4**, 15–21 (2013).
3. Lim, S. H., Kathuria, H., Tan, J. J. Y. & Kang, L. 3D printed drug delivery and testing systems - a passing fad or the future? *Adv. Drug Deliv. Rev.* **132**, 139–168 (2018).
4. Habibovic, P. *et al.* Osteoconduction and osteoinduction of low-temperature 3D printed bioceramic implants. *Biomaterials* **29**, 944–953 (2008).
5. Hockaday, L. A. *et al.* Rapid 3D printing of anatomically accurate and mechanically heterogeneous aortic valve hydrogel scaffolds. *Biofabrication* **4**, 035005 (2012).
6. Morrison, R. J. *et al.* Mitigation of tracheobronchomalacia with 3D-printed personalized medical devices in pediatric patients. *Sci. Transl. Med.* **7**, 285ra64 (2015).
7. ten Kate, J., Smit, G. & Breedveld, P. 3D-printed upper limb prostheses: a review. *Disabil. Rehabil. Assist. Technol.* **12**, 300–314 (2017).

8. Robinson, S. S. *et al.* Patient-specific design of a soft occluder for the left atrial appendage. *Nature Biomedical Engineering* **2**, 8–16 (2018).
9. Melchels, F. P. W., Feijen, J. & Grijpma, D. W. A review on stereolithography and its applications in biomedical engineering. *Biomaterials* **31**, 6121–6130 (2010).
10. Gibson, I., Rosen, D. & Stucker, B. *Additive Manufacturing Technologies: 3D Printing, Rapid Prototyping, and Direct Digital Manufacturing*. (Springer, 2014).
11. Giannatsis, J. & Dedoussis, V. Additive fabrication technologies applied to medicine and health care: a review. *Int. J. Adv. Manuf. Technol.* **40**, 116–127 (2009).
12. Minas, C., Carnelli, D., Tervoort, E. & Studart, A. R. 3D Printing of Emulsions and Foams into Hierarchical Porous Ceramics. *Adv. Mater.* **28**, 9993–9999 (2016).
13. Nguyen, D. T. *et al.* 3D-Printed Transparent Glass. *Adv. Mater.* **29**, (2017).
14. Kirchmajer, D. M., Gorkin, R., III & in het Panhuis, M. An overview of the suitability of hydrogel-forming polymers for extrusion-based 3D-printing. *J. Mater. Chem. B Mater. Biol. Med.* **3**, 4105–4117 (2015).
15. Chia, H. N. & Wu, B. M. Recent advances in 3D printing of biomaterials. *J. Biol. Eng.* **9**, 4 (2015).
16. Tiwari, A., Salacinski, H. J., Punshon, G., Hamilton, G. & Seifalian, A. M. Development of a hybrid cardiovascular graft using a tissue engineering approach. *FASEB J.* **16**, 791–796 (2002).
17. Vrancken, A. C. T. *et al.* Short Term Evaluation of an Anatomically Shaped Polycarbonate Urethane Total Meniscus Replacement in a Goat Model. *PLoS One* **10**, e0133138 (2015).
18. Sun, J.-Y. *et al.* Highly stretchable and tough hydrogels. *Nature* **489**, 133–136 (2012).
19. Miller, A. T. *et al.* Fatigue of injection molded and 3D printed polycarbonate urethane in

solution. *Polymer* **108**, 121–134 (2017).

20. Ngo, T. D., Kashani, A., Imbalzano, G., Nguyen, K. T. Q. & Hui, D. Additive manufacturing (3D printing): A review of materials, methods, applications and challenges. *Composites Part B* **143**, 172–196 (2018).
21. Van de Velde, K. & Kiekens, P. Biopolymers: overview of several properties and consequences on their applications. *Polym. Test.* **21**, 433–442 (2002).
22. Truby, R. L. & Lewis, J. A. Printing soft matter in three dimensions. *Nature* **540**, 371–378 (2016).
23. Lee, J.-Y., An, J. & Chua, C. K. Fundamentals and applications of 3D printing for novel materials. *Applied Materials Today* **7**, 120–133 (2017).
24. Shanks, R. A. & Kong, I. General Purpose Elastomers: Structure, Chemistry, Physics and Performance. in *Advances in Elastomers I: Blends and Interpenetrating Networks* (eds. Visakh, P. M., Thomas, S., Chandra, A. K. & Mathew, A. P.) 11–45 (Springer Berlin Heidelberg, 2013).
25. De, S. K. *Rubber Technologist's Handbook*. (Smithers Rapra Press, 2001).
26. Gennisson, J.-L. *et al.* Viscoelastic and anisotropic mechanical properties of in vivo muscle tissue assessed by supersonic shear imaging. *Ultrasound Med. Biol.* **36**, 789–801 (2010).
27. Pinto, J. G. & Fung, Y. C. Mechanical properties of the heart muscle in the passive state. *J. Biomech.* **6**, 597–616 (1973).
28. Trubel, W. *et al.* Compliance mismatch and formation of distal anastomotic intimal hyperplasia in externally stiffened and lumen-adapted venous grafts. *Eur. J. Vasc. Endovasc. Surg.* **10**, 415–423 (1995).
29. Harris, J. P. *et al.* Mechanically adaptive intracortical implants improve the proximity of

neuronal cell bodies. *J. Neural Eng.* **8**, 066011 (2011).

30. Schouman, T., Schmitt, M., Adam, C., Dubois, G. & Rouch, P. Influence of the overall stiffness of a load-bearing porous titanium implant on bone ingrowth in critical-size mandibular bone defects in sheep. *J. Mech. Behav. Biomed. Mater.* **59**, 484–496 (2016).
31. Scharfschwerdt, M. *et al.* In vitro investigation of a novel elastic vascular prosthesis for valve-sparing aortic root and ascending aorta replacement. *Eur. J. Cardiothorac. Surg.* **49**, 1370–1373 (2016).
32. Nezarati, R. M., Eifert, M. B., Dempsey, D. K. & Cosgriff-Hernandez, E. Electrospun vascular grafts with improved compliance matching to native vessels. *J. Biomed. Mater. Res. B Appl. Biomater.* **103**, 313–323 (2015).
33. Hepburn, C. *Polyurethane Elastomers*. (Springer Science & Business Media, 2012).
34. Akindoyo, J. O. *et al.* Polyurethane types, synthesis and applications – a review. *RSC Adv.* **6**, 114453–114482 (2016).
35. Oprea, S. Effect of Composition and Hard-segment Content on Thermo-mechanical Properties of Cross-linked Polyurethane Copolymers. *High Perform. Polym.* **21**, 353–370 (2009).
36. Kultys, A., Rogulska, M., Pikus, S. & Skrzypiec, K. The synthesis and characterization of new thermoplastic poly(carbonate-urethane) elastomers derived from HDI and aliphatic–aromatic chain extenders. *Eur. Polym. J.* **45**, 2629–2643 (2009).
37. Eceiza, A. *et al.* Thermoplastic polyurethane elastomers based on polycarbonate diols with different soft segment molecular weight and chemical structure: Mechanical and thermal properties. *Polym. Eng. Sci.* **48**, 297–306 (2008).
38. Christenson, E. M., Anderson, J. M. & Hiltner, A. Biodegradation mechanisms of

polyurethane elastomers. *Corros. Eng. Sci. Technol.* **42**, 312–323 (2007).

39. Wiggins, M. J., Wilkoff, B., Anderson, J. M. & Hiltner, A. Biodegradation of polyether polyurethane inner insulation in bipolar pacemaker leads. *J. Biomed. Mater. Res.* **58**, 302–307 (2001).
40. Mathur, A. B. *et al.* In vivo biocompatibility and biostability of modified polyurethanes. *J. Biomed. Mater. Res.* **36**, 246–257 (1997).
41. Healy, K., Hutmacher, D. W., Grainger, D. W. & James Kirkpatrick, C. *Comprehensive Biomaterials II*. (Elsevier, 2017).
42. Hergenrother, R. W., Xue-Hai, Y. & Cooper, S. L. Blood-contacting properties of polydimethylsiloxane polyurea urethanes. *Biomaterials* **15**, 635–640 (1994).
43. Gasparotti, E. *et al.* A 3D printed melt-compounded antibiotic loaded thermoplastic polyurethane heart valve ring design: an integrated framework of experimental material tests and numerical simulations. *International Journal of Polymeric Materials and Polymeric Biomaterials* **68**, 1–10 (2019).
44. ASTM International. *ASTM D638-14, Standard Test Method for Tensile Properties of Plastics*. www.astm.org.
45. ISO. *ISO 10993-5. Biological evaluation of medical devices -- Part 5: Tests for in vitro cytotoxicity*. (2009).
46. Knetsch, M. L. W., Olthof, N. & Koole, L. H. Polymers with tunable toxicity: a reference scale for cytotoxicity testing of biomaterial surfaces. *J. Biomed. Mater. Res. A* **82**, 947–957 (2007).
47. Dongdong, P. & Hengshui, T. Polycarbonate polyurethane elastomers synthesized via a solvent-free and nonisocyanate melt transesterification process. *J. Appl. Polym. Sci.* **132**,

(2015).

48. Coogan, T. J. & Kazmer, D. O. In-line rheological monitoring of fused deposition modeling. *J. Rheol.* **63**, 141–155 (2019).
49. Choong, G. Y. H., De Focatiis, D. S. A. & Hassell, D. G. Viscoelastic melt rheology and time–temperature superposition of polycarbonate–multi-walled carbon nanotube nanocomposites. *Rheol. Acta* **52**, 801–814 (2013).
50. Ramirez, J. & Boudara, V. *Rheology of Entangled Polymers: Toolkit for Analysis of Theory and Experiment*. (2018).
51. Xu, X., Chen, J. & An, L. Shear thinning behavior of linear polymer melts under shear flow via nonequilibrium molecular dynamics. *J. Chem. Phys.* **140**, 174902 (2014).
52. Sun, Q., Rizvi, G. M., Bellehumeur, C. T. & Gu, P. Effect of processing conditions on the bonding quality of FDM polymer filaments. *Rapid Prototyping Journal* (2013) doi:10.1108/13552540810862028.
53. Coogan, T. J. & Kazmer, D. O. Bond and part strength in fused deposition modeling. *Rapid Prototyping Journal* (2017) doi:10.1108/RPJ-03-2016-0050.
54. Bellehumeur, C., Li, L., Sun, Q. & Gu, P. Modeling of Bond Formation Between Polymer Filaments in the Fused Deposition Modeling Process. *J. Manuf. Process.* **6**, 170–178 (2004).
55. Aliheidari, N., Tripuraneni, R., Ameli, A. & Nadimpalli, S. Fracture resistance measurement of fused deposition modeling 3D printed polymers. *Polym. Test.* **60**, 94–101 (2017).
56. Davis, C. S., Hillgartner, K. E., Han, S. H. & Seppala, J. E. Mechanical strength of welding zones produced by material extrusion additive manufacturing. *Addit Manuf* **16**, 162–166

(2017).

57. Seppala, J. E. & Migler, K. D. Infrared thermography of welding zones produced by polymer extrusion additive manufacturing. *Addit Manuf* **12**, 71–76 (2016).

58. Bagley, E. B. & Schreiber, H. P. Effect of Die Entry Geometry on Polymer Melt Fracture and Extrudate Distortion. *Transactions of the Society of Rheology* **5**, 341–353 (1961).

59. Nason, H. K. A High Temperature, High Pressure Rheometer for Plastics. *J. Appl. Phys.* **16**, 338–343 (1945).

60. Dinwiddie, R. B. *et al.* Infrared imaging of the polymer 3D-printing process. in *Thermosense: Thermal Infrared Applications XXXVI* vol. 9105 910502 (International Society for Optics and Photonics, 2014).

61. Hsu, S.-H., Yen, H.-J., Tseng, C.-S., Cheng, C.-S. & Tsai, C.-L. Evaluation of the growth of chondrocytes and osteoblasts seeded into precision scaffolds fabricated by fused deposition manufacturing. *J. Biomed. Mater. Res. B Appl. Biomater.* **80**, 519–527 (2007).

62. Yen, H.-J., Tseng, C.-S., Hsu, S.-H. & Tsai, C.-L. Evaluation of chondrocyte growth in the highly porous scaffolds made by fused deposition manufacturing (FDM) filled with type II collagen. *Biomed. Microdevices* **11**, 615–624 (2009).

63. Agarwala, M. K. *et al.* Structural quality of parts processed by fused deposition. *Rapid Prototyping Journal* **2**, 4–19 (1996).

64. Bellini, A., Güçeri, S. & Bertoldi, M. Liquefier Dynamics in Fused Deposition. *J. Manuf. Sci. Eng.* **126**, 237–246 (2004).

65. Carneiro, O. S., Silva, A. F. & Gomes, R. Fused deposition modeling with polypropylene. *Mater. Des.* **83**, 768–776 (2015).

66. Spoerk, M., Gonzalez-Gutierrez, J., Sapkota, J., Schuschnigg, S. & Holzer, C. Effect of the

printing bed temperature on the adhesion of parts produced by fused filament fabrication. *Plast. Rubber Compos. Process. Appl.* **47**, 17–24 (2018).

67. Wiggins, M. J., MacEwan, M., Anderson, J. M. & Hiltner, A. Effect of soft-segment chemistry on polyurethane biostability during in vitro fatigue loading. *J. Biomed. Mater. Res.* **68A**, 668–683 (2004).
68. Wu, W. *et al.* Influence of Layer Thickness and Raster Angle on the Mechanical Properties of 3D-Printed PEEK and a Comparative Mechanical Study between PEEK and ABS. *Materials* **8**, 5834–5846 (2015).
69. Huang, B. & Singamneni, S. Raster angle mechanics in fused deposition modelling. *J. Compos. Mater.* **49**, 363–383 (2015).
70. Christenson, E. M., Dadsetan, M., Wiggins, M., Anderson, J. M. & Hiltner, A. Poly(carbonate urethane) and poly(ether urethane) biodegradation: in vivo studies. *J. Biomed. Mater. Res. A* **69**, 407–416 (2004).
71. Christenson, E. M., Anderson, J. M. & Hiltner, A. Oxidative mechanisms of poly(carbonate urethane) and poly(ether urethane) biodegradation:In vivo andin vitro correlations. *J. Biomed. Mater. Res.* **70A**, 245–255 (2004).
72. Christenson, E. M., Dadsetan, M., Anderson, J. M. & Hiltner, A. Biostability and macrophage-mediated foreign body reaction of silicone-modified polyurethanes. *J. Biomed. Mater. Res.* **74A**, 141–155 (2005).
73. Dempsey, D. K. *et al.* Comparative analysis of in vitro oxidative degradation of poly(carbonate urethanes) for biostability screening. *J. Biomed. Mater. Res. A* **102**, 3649–3665 (2014).
74. 17 yo Female, Normal Heart (sliced sagittally) | NIH 3D Print Exchange.

https://3dprint.nih.gov/discover/3dpx-007207.

SUPPORTING INFORMATION

S1. Printing parameters used for the quasistatic tensile test experiments

For quasistatic tensile testing, the same printing parameters were used for all samples, as summarized in **Table S1**. This parameter resulted in high-quality, repeatable prints, as indicated by dogbone samples with minimal voids and high dimensional fidelity. Although there are many more parameters that can be listed here, they are deemed to be of minimal effect to the final fabricated object.

Table S1. Printing parameters used for the quasistatic tensile test experiments.

Printing Speed	4 mm/second
Nozzle Temperature	260 °C
Bed Temperature	50 °C
Extrusion Multiplier	1.3
Layer Height	0.15 mm
Layer Width	0.35 mm
Raster Angle	0° (perpendicular to dogbone's longest axis)
Infill	100%
Perimeter Overlap	15%
Shell	0.3 mm × 2

S2. Calculation of volumetric flow

The volumetric flow rate of the polymer melt through the nozzle is estimated as Eq. (S1):

$$Q = V \times \pi \times {h_{layer}}^2 \quad \text{(S1)}$$

where Q is the volumetric flow rate, V is the printing speed, and h_{layer} is the layer height.

The apparent shear rate can be estimated from Eq. (S2):

$$\Gamma = \frac{4Q}{\pi R_{nozzle}^{\ 3}} \qquad \text{(S2)}$$

where Γ is the uncorrected apparent shear rate[48]. Assuming a 0.35 mm nozzle size and a printing speed ranging from 1 mm/s to 50 mm/s, an estimate for the uncorrected apparent shear rate can be calculated.

S3. Time-temperature superposition of rheological data

The complex viscosity of the polymer melt is estimated via temperature-time superposition (TTS)[49]. Master curves using Arrhenius relation were constructed for the temperatures studied using RepTate[50] to determine the viscosities at higher angular frequencies. The resulting master curve for a reference temperature of 260 °C is shown by **Fig. 2** in Results and Discussion. Shift factor values used for TTS is shown in **Table S2**. Raw viscosity measurement data at various temperatures is shown in **Fig S1.**

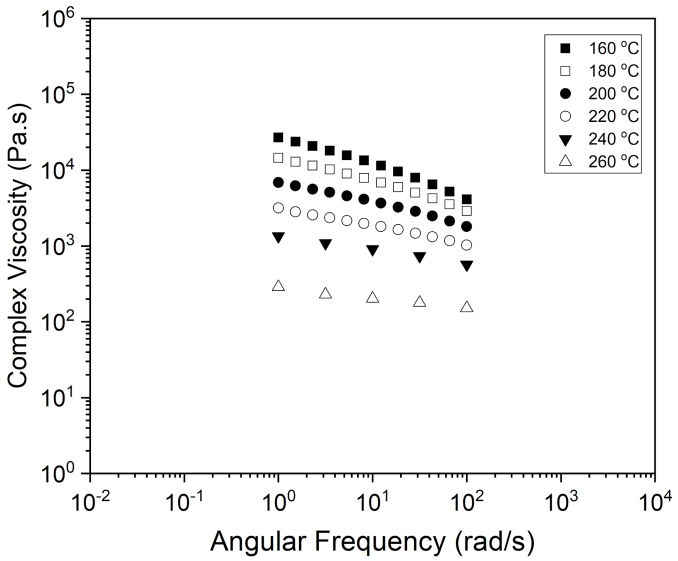

Figure S1. Raw rheological measurement data done at various temperatures.

Table S2. Vertical and horizontal shift factors used for TTS to 260 °C reference temperature.

T (°C)	**log(H_{shift})**	**log(V_{shift})**
160	3.55	0.93
180	3.11	0.879
200	2.53	0.754
220	1.79	0.516
240	1.13	0.304
260	0	0

S4. Printing parameters and corresponding results

MicroCT cross-section of printed samples was evaluated for under/over extrusion, porosity, and geometric deviation as summarized in **Table S2**. To calculate over/under-extrusion, an area of interest was generated from the microCT data with a size of 2.79 mm x 3 mm, meaning the predicted volume using the predetermined print setting should be as Eq. (S3):

$$W \times L \times t \times F_{multi} = 2.79 \times 3 \times 0.35 \times 1.3 = 3.81\ mm^3 \quad \text{(S3)}$$

wherein W is the width, L is the length, t is the thickness, and F_{multi} is the extrusion multiplier. Geometric variance evaluation was shown by **Fig S1**. Porosity is calculated by thresholding the reconstructed 3D model and evaluating porosity using analysis software, CTan (Bruker microCT, Billerica, MA).

S5. Image processing for variance calculation

For the calculation of geometric variance, the following steps were used:

1) The cross-section was converted into black and white via thresholding (**Fig. S1-a**).

2) Thickness was measured over the length of the printed line (**Fig. S1-b**)

3) The variance of this thickness was calculated after tilt adjustment and used as a variance of the printed object's cross-section (**Fig. S1-c**).

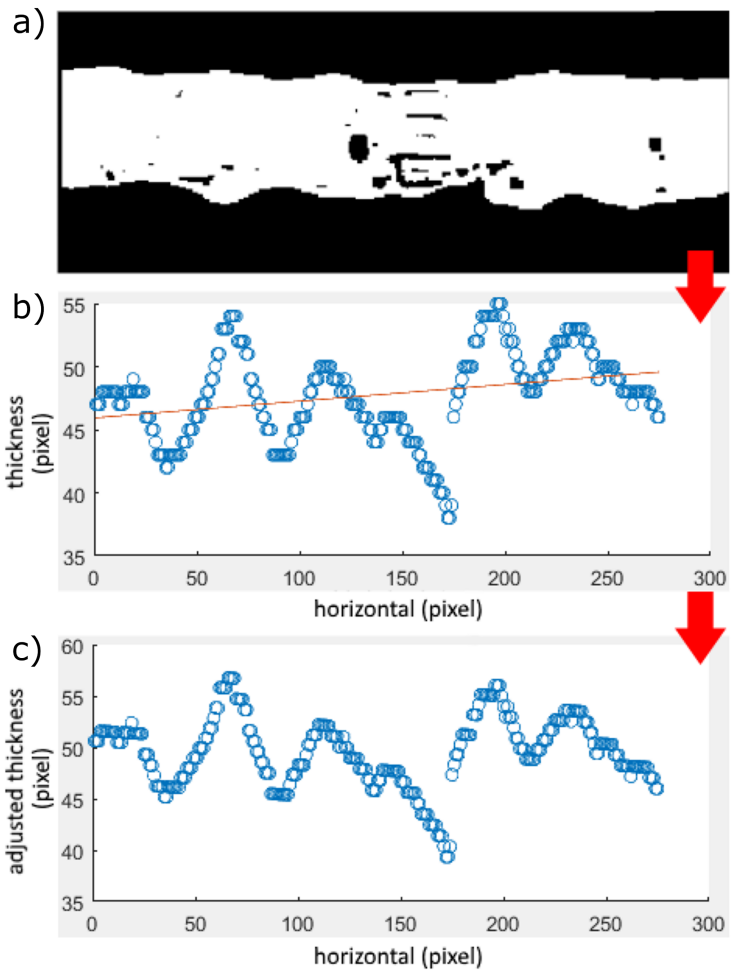

Fig S2. Example of image processing for variance calculation. a) The cross-section image converted into a black-white image using MATLAB's im2bw function with a thresholding level of 0.3. The uppermost and bottommost white pixel in the vertical direction is detected as the top and bottom edge, respectively. b) Thickness measured over the length of the printed line. The red line shows the regression line used for image tilt adjustment c) Thickness after tilt-adjustment. The variance of this thickness was calculated and used as a "variance" of the printed object's cross-section.

Table S2. Printing parameters and its corresponding result.

Printing Parameter			Volume (mm^3)	Under- or Over-Extrusion (%)	Porosity (%)	Geometric Variance (μm)
Layer Height (mm)	Temperature (ºC)	Print Speed (mm/s)				
0.3	240	1	3.66	96.06	0.30	45.7
		5	1.84	48.29	0.00	73.8
	260	5	3.69	94.22	0.00	61.1
		9	2.92	76.74	0.00	59.4
		17	2.19	57.48	0.00	62.9
	280	5	3.66	96.06	1.86	3.62
		9	3.75	98.42	0.56	4.61
0.15	240	1	3.93	103.13	1.02	67.0
		5	3.72	97.37	0.04	90.8
		9	4.48	117.58	0.02	72.7
	260	5	3.51	92.12	1.19	38.5
		9	3.56	93.43	0.06	25.0
		17	3.49	91.60	0.04	64.0
	280	9	3.85	101.04	1.53	33.8
		17	3.66	96.06	2.46	61.7
0.05	240	5	3.77	98.95	0.23	21.0
	260	9	3.64	95.53	0.18	57.2

S5. Effects of aging on 3D-printed PCU-Sil samples

Aged 3D-printed PCU-Sil samples exhibited a change in mechanical properties over time as **Fig. S2**. This change appeared to stop after 14 days. Based on the results, samples were aged for 14 days in a desiccator before the measurement for comparing the effects of different printing conditions to minimize aging effects.

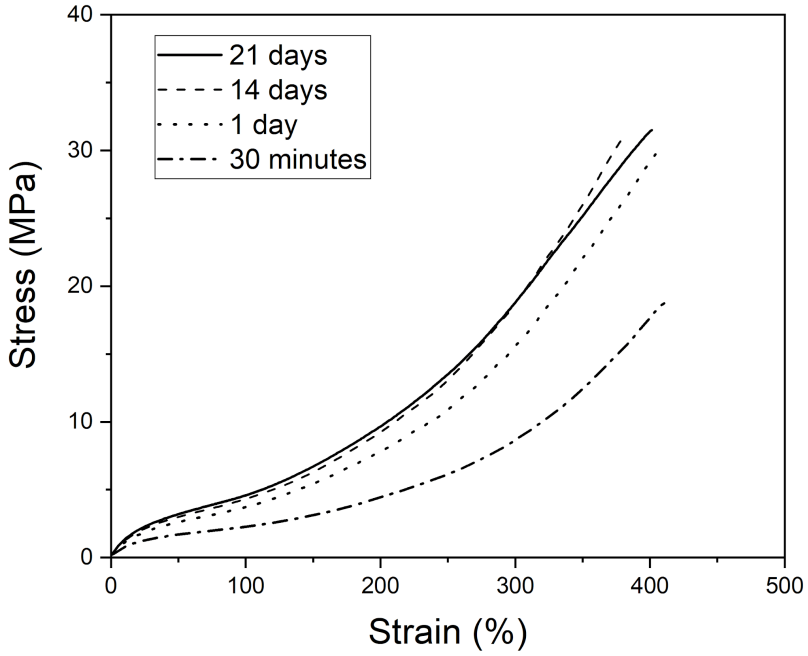

Fig S3. Representative stress-strain curves of aged 3D-printed PCU-Sil samples. The time in the legend indicates the aging time.

SUPPORTING INFORMATION

S1. Printing parameters used for the quasistatic tensile test experiments

For quasistatic tensile testing, the same printing parameters were used for all samples, as summarized in **Table S1**. This parameter resulted in high-quality, repeatable prints, as indicated by dogbone samples with minimal voids and high dimensional fidelity. Although there are many more parameters that can be listed here, they are deemed to be of minimal effect to the final fabricated object.

Table S1. Printing parameters used for the quasistatic tensile test experiments.

Printing Speed	4 mm/second
Nozzle Temperature	260 °C
Bed Temperature	50 °C
Extrusion Multiplier	1.3
Layer Height	0.15 mm
Layer Width	0.35 mm
Raster Angle	0° (perpendicular to dogbone's longest axis)
Infill	100%
Perimeter Overlap	15%
Shell	0.3 mm × 2

S2. Calculation of volumetric flow

The volumetric flow rate of the polymer melt through the nozzle is estimated as Eq. (S1):

$$Q = V \times \pi \times h_{layer}{}^{2} \quad \text{(S1)}$$

where Q is the volumetric flow rate, V is the printing speed, and h_{layer} is the layer height.

The apparent shear rate can be estimated from Eq. (S2):

$$\Gamma = \frac{4Q}{\pi R_{nozzle}^{\ 3}} \qquad \text{(S2)}$$

where Γ is the uncorrected apparent shear rate[48]. Assuming a 0.35 mm nozzle size and a printing speed ranging from 1 mm/s to 50 mm/s, an estimate for the uncorrected apparent shear rate can be calculated.

S3. Time-temperature superposition of rheological data

The complex viscosity of the polymer melt is estimated via temperature-time superposition (TTS)[49]. Master curves using Arrhenius relation were constructed for the temperatures studied using RepTate[50] to determine the viscosities at higher angular frequencies. The resulting master curve for a reference temperature of 260 °C is shown by **Fig. 2** in Results and Discussion. Shift factor values used for TTS is shown in **Table S2**. Raw viscosity measurement data at various temperatures is shown in **Fig S1.**

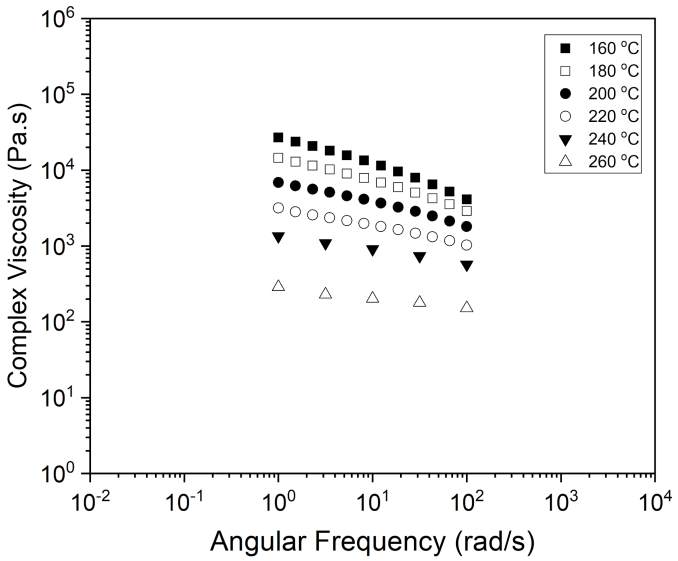

Figure S1. Raw rheological measurement data done at various temperatures.

Table S2. Vertical and horizontal shift factors used for TTS to 260 °C reference temperature.

T (°C)	**log(H_{shift})**	**log(V_{shift})**
160	3.55	0.93
180	3.11	0.879
200	2.53	0.754
220	1.79	0.516
240	1.13	0.304
260	0	0

S4. Printing parameters and corresponding results

MicroCT cross-section of printed samples was evaluated for under/over extrusion, porosity, and geometric deviation as summarized in **Table S2**. To calculate over/under-extrusion, an area of interest was generated from the microCT data with a size of 2.79 mm x 3 mm, meaning the predicted volume using the predetermined print setting should be as Eq. (S3):

$$W \times L \times t \times F_{multi} = 2.79 \times 3 \times 0.35 \times 1.3 = 3.81\ mm^3 \quad \text{(S3)}$$

wherein W is the width, L is the length, t is the thickness, and F_{multi} is the extrusion multiplier. Geometric variance evaluation was shown by **Fig S1**. Porosity is calculated by thresholding the reconstructed 3D model and evaluating porosity using analysis software, CTan (Bruker microCT, Billerica, MA).

S5. Image processing for variance calculation

For the calculation of geometric variance, the following steps were used:

1) The cross-section was converted into black and white via thresholding (**Fig. S1-a**).

2) Thickness was measured over the length of the printed line (**Fig. S1-b**)

3) The variance of this thickness was calculated after tilt adjustment and used as a variance of the printed object's cross-section (**Fig. S1-c**).

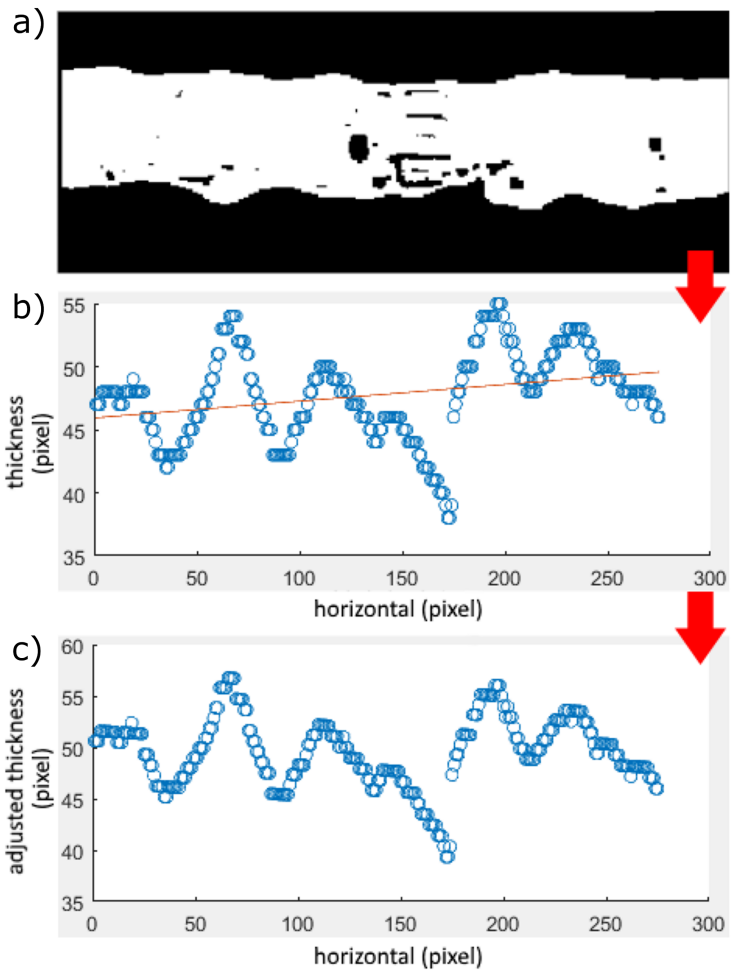

Fig S2. Example of image processing for variance calculation. a) The cross-section image converted into a black-white image using MATLAB's im2bw function with a thresholding level of 0.3. The uppermost and bottommost white pixel in the vertical direction is detected as the top and bottom edge, respectively. b) Thickness measured over the length of the printed line. The red line shows the regression line used for image tilt adjustment c) Thickness after tilt-adjustment. The variance of this thickness was calculated and used as a "variance" of the printed object's cross-section.

Table S2. Printing parameters and its corresponding result.

Printing Parameter			Volume (mm^3)	Under- or Over-Extrusion (%)	Porosity (%)	Geometric Variance (μm)
Layer Height (mm)	Temperature (ºC)	Print Speed (mm/s)				
0.3	240	1	3.66	96.06	0.30	45.7
		5	1.84	48.29	0.00	73.8
	260	5	3.69	94.22	0.00	61.1
		9	2.92	76.74	0.00	59.4
		17	2.19	57.48	0.00	62.9
	280	5	3.66	96.06	1.86	3.62
		9	3.75	98.42	0.56	4.61
0.15	240	1	3.93	103.13	1.02	67.0
		5	3.72	97.37	0.04	90.8
		9	4.48	117.58	0.02	72.7
	260	5	3.51	92.12	1.19	38.5
		9	3.56	93.43	0.06	25.0
		17	3.49	91.60	0.04	64.0
	280	9	3.85	101.04	1.53	33.8
		17	3.66	96.06	2.46	61.7
0.05	240	5	3.77	98.95	0.23	21.0
	260	9	3.64	95.53	0.18	57.2

S5. Effects of aging on 3D-printed PCU-Sil samples

Aged 3D-printed PCU-Sil samples exhibited a change in mechanical properties over time as **Fig. S2**. This change appeared to stop after 14 days. Based on the results, samples were aged for 14 days in a desiccator before the measurement for comparing the effects of different printing conditions to minimize aging effects.

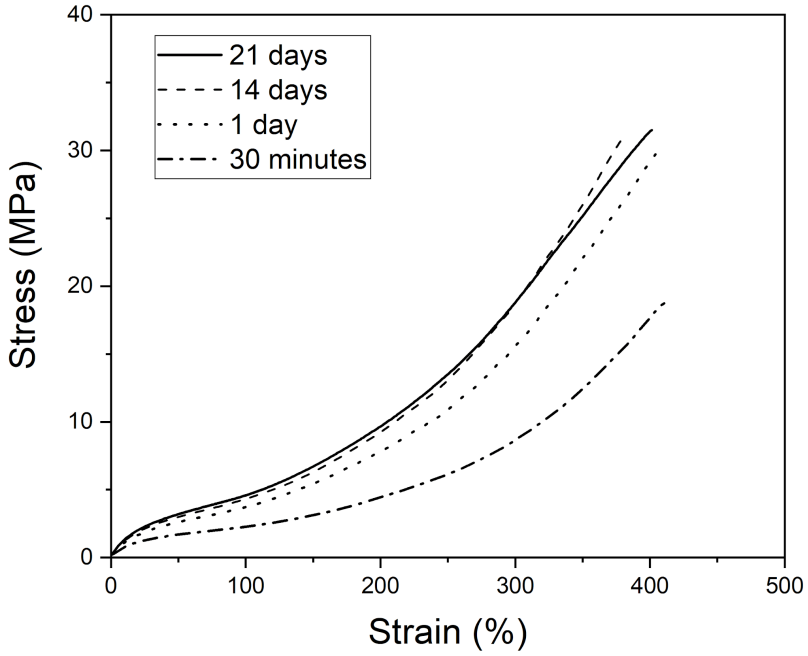

Fig S3. Representative stress-strain curves of aged 3D-printed PCU-Sil samples. The time in the legend indicates the aging time.